# Grain size mediated electrical and thermoelectric performances of mechanically alloyed $Sb_2Te_3$ nanoparticles

Shrabani Paul [a], Umapada Pal [b], Swapan Kumar Pradhan [a, *]

[a] Department of Physics, The University of Burdwan, Golapbag, Burdwan, 713104, West Bengal, India
[b] Instituto de Fisica, Benemérita Universidad Autónoma de Puebla, Apdo. Postal J-48, Puebla, Pue.72570, Mexico

## ARTICLE INFO

## ABSTRACT

Antimony telluride ($Sb_2Te_3$) nanoparticles of different sizes were fabricated by mechanical alloying (MA) of elemental Sb and Te powers for different durations. The powder nanostructures were pelletized, annealed in Ar ambient, and characterized by XRD, FESEM, TEM to study the effect of milling time and thermal treatment on particle size, grain growth, and crystallinity. The annealed and unannealed pelletized nanostructures were analyzed in a PPMS to study the effect of grain growth on their electrical and thermoelectric properties. Room temperature electrical conductivity of the p-type semiconductor nanostructures improved significantly (from ~$10^3$ to ~ $10^5$ mho/m) due to thermal annealing and results in the considerable improvement in thermoelectric figure of merit (ZT). Thermal annealing-induced grain growth also transforms the semiconducting nature of the sample to metallic. The reduced thermal conductivity of the nanostructures with reduced grain size improves the ZT. The temperature-dependent Lorenz number ($L_{effective}$) is used to find the electronic contribution of total thermal conductivity, and it is explained by the non-parabolic Kane model.

## 1. Introduction

Thermoelectric materials are efficient converters of waste heat into useable electrical energy due to their high Seebeck coefficients [1,2]. Thermoelectric figure of merit ZT defines the performance of a thermoelectric material in converting thermal energy to electricity. The ZT is defined as, $ZT = S^2\sigma T/K$, where S,$\sigma$, and K represent the Seebeck coefficient, electrical conductivity, the thermal conductivity of the material, respectively, and T is the temperature in K [3]. The $S^2\sigma$ term is defined as the power factor. Owing to the demand for alternative energy sources, the quest for new materials with an improved figure of merit (ZT) has increased globally at a rapid rate [4,5].

In general, semiconductors are better thermoelectric materials compared to metals [6]. According to Wiedemann-Franz law [7], most metals have a nearly constant electrical to thermal conductivity ratio, and increasing electrical conductivity is difficult without increasing their thermal conductivity. However, a good ZT value requires a high electrical conductivity and simultaneously a lower thermal conductivity. Hence, for metals or metallic alloys, the only possible way to obtain a significant figure of merit is to have a high value of the Seebeck coefficient. Unfortunately, most metals show very small Seebeck coefficients (~10 $\mu$V/K), and their thermoelectric efficiencies are only fractions of a percent. On the other hand, semiconductors with comparatively higher Seebeck coefficient values (~100 $\mu$V/K) had drawn strong attention as thermoelectric materials since 1920 [8]. Low bandgap semiconductors possess high electrical conductivity, comparable to metals. Compared to bulk materials, nanomaterials have low thermal conductivity because of lower lattice thermal conductivity resulting from the increased phonon scattering due to smaller grain size [9–12]. Thus, nanostructured semiconductors of smaller bandgaps are considered the most favorable thermoelectric materials as they produce a reasonably higher figure of merit values.

Antimony telluride ($Sb_2Te_3$), a low bandgap semiconductor, has been considered as one of the promising thermoelectric materials for low-temperature applications [13–15]. Nano-structured $Sb_2Te_3$ thin films fabricated by physical vapor deposition [16], metal-organic chemical vapor deposition [17,18], thermal co-evaporation [19], flash evaporation [20], electrochemical method [21], ion beam sputtering [22], molecular beam epitaxy [23] etc. have shown good thermoelectric conversion efficiency. On the other hand, single-phase $Sb_2Te_3$ nanoparticles synthesized by microwave-assisted

decomposition of the single-source precursor [24], chemical synthetic process [25], and mechanical alloying (MA) [26] have also been tested for thermoelectric applications. Among them, the primary advantages of the mechanical alloying method are its simplicity, ability to produce nanoparticles in a short duration of time with the least number of starting materials, and easy control over their crystallite size. The nanoparticles synthesized by the mechanical alloying process have also shown good thermoelectric behaviors [27–32]. However, there are hardly very few works where the phase pure $Sb_2Te_3$ nanoparticles have been fabricated by mechanical alloying [26]. So, there is a large scope to explore the thermoelectric behavior of pure $Sb_2Te_3$ phase synthesized by facile and time-efficient MA process. Again, as the grain size of nanoparticles plays an important role in their thermoelectric performance, several reports have been published in the literature studying the grain size effect on thermoelectric properties of $Sb_2Te_3$ [13,33–35] and its alloys [36,37]. Since the nanomaterials synthesized by mechanical alloying contain significant lattice imperfections and pores, a post-growth thermal treatment is necessary to reduce the porosity and defects in these nanostructures [38] to enhance their electrical conductivity. Thermal treatments such as hot pressing, annealing in an inert ambient and spark plasma sintering (SPS) have been utilized on fabricated semiconductor nanostructures to improve electrical conductivity and their effect on several transport properties of nanostructured $Sb_2Te_3$ [26,39] and its alloys [27,35,40–43] have been studied.

The effect of grain size and film thickness on thermal and electrical transport properties of $Sb_2Te_3$ thin films have been studied earlier [13,33–35]. However, the grain size effect of spherical nanocrystallites on thermal and electrical transport properties of $Sb_2Te_3$ powdered sample has not been studied yet. Thus, the primary purposes of the present work are, (i) to explain in details the spherical grain size effect on thermoelectric properties of the nanocrystalline single-phase $Sb_2Te_3$ synthesized within a record short duration of 3 h, employing MA (first reported here), and (ii) to study the effect of heat treatment of the sample on different transport properties in the context of grain growth. This article also deals with the modified Lorenz number ($L_{effective}$), which changes with temperature to calculate electronic thermal conductivity, which lowers its value much from the value calculated with constant Lorenz number ($L_0 = 2.45 \times 10^{-8}$ W$\Omega$/K$^2$) in the theoretical limit. The non-parabolic Kane model is considered in this context. The wide temperature variations of total thermal conductivity along with electronic and lattice thermal conductivity, as well as Lorenz number of $Sb_2Te_3$ nanocrystals having different sizes, are described elaborately for the first time in this work.

In this article, we present the one-step fabrication of single-phase $Sb_2Te_3$ nanoparticles of almost spherical morphology by mechanical alloying of elemental precursors within only 3 h of duration. The structure and microstructure characterizations of synthesized ball-milled nanoparticles before and after thermal annealing have been done employing Rietveld refinement of X-ray diffraction (XRD) pattern, analyzing field-emission scanning electron microscope (FESEM) and transmission electron microscope (TEM) images. The Fourier-transform infrared (FTIR) spectra reveal the bandgap measurements of milled and annealed samples. All the thermal and electric transport properties are measured using a physical property measurement system (PPMR) to observe the effects of alloying time and thermal annealing on the transport properties of the $Sb_2Te_3$ nanostructures. We demonstrate that the electrical conductivity of the nanostructures can be enhanced significantly by thermal annealing. Utilizing the non-parabolic Kane model, we have described how the effective Lorenz number ($L_{effective}$) contributed to the electronic and lattice components of thermal conductivity of the nanostructures, and hence on their figure of merit.

## 2. Experimental

### 2.1. Material synthesis

For the fabrication of $Sb_2Te_3$ nanostructures by MA, a stoichiometric mixture of Sb (99%, SRL) and Te (99.8%, Sigma-Aldrich) metal powders were taken in a chrome steel bowl of 80 ml volume containing 30 chrome steel balls of 10 mm diameter each under Ar atmosphere and sealed hermetically. The powder mixture was then milled in a planetary ball mill (P6, M/S Fritsch, GmbH, Germany) with a ball to powder mass ratio 40:1 for 1 h, 3 h, 5 h, and 10 h durations. After each 15 min, the milling process was paused for 15 min to keep the bowl temperature well below the melting temperatures of the metal powders and avoid contamination from milling media. The milled powders were collected and cold-pressed in a hydraulic press uni-axially to form pellets under a pressure of 5 ton for 15 min in stainless steel die of 13 mm diameter. An equal amount (600 mg) of each of the powder samples was taken for pelletization to obtain compact pellets of 13 mm diameter and similar thickness. All the pelletized samples were annealed at 573 K for 6 h under the Ar atmosphere inside a carbolite horizontal furnace. The temperature of the furnace was increased at 2°C/min, and the Ar gas flow was maintained at 120 cc/min. The thickness of the thermally treated pellets were 1.18, 0.98, and 0.88 mm for 3 h, 5 h, 10 h milled samples, respectively.

### 2.2. Material characterization

Structure and microstructure characterizations of the unmilled, all ball milled, and annealed pellet samples were carried out by analyzing their X-ray diffraction (XRD) patterns recorded using Cu K$_\alpha$ radiation (1.5406 Å) of a Bruker AXS, D8 Advance diffractometer operating at 40 kV and 40 mA. The XRD patterns were recorded from 20° to 80° 2θ range in step scan mode, with a step size of 0.02° and scanning time of 2s/step. For morphology and fine structure analysis of the samples, they were analyzed in a field-emission scanning electron microscope (FESEM, ZEISS, Sigma 300) and a transmission electron microscope (TEM, JEOL, JEM 1400 plus). For composition and element distribution analysis, EDX spectra of the samples were recorded in the ZEISS microscope attached to Ametek analytical system.

The Fourier-transform infrared (FTIR) spectra of representative $Sb_2Te_3$ samples (10 h milled samples) were recorded before and after thermal treatment to study the effect of thermal treatment on bandgap and chemical bonding. For recording the FTIR spectra of the samples, a tiny amount of sample was mixed with dry KBr (with a mass ratio 1:40), well ground in an agate mortar for 10 min and pelletized in a hydraulic press, under 1000 kg/cm$^2$ pressure for 10 min and analyzed in a Perkin-Elmer (FRONTIER) spectrometer in the 400-4000 cm$^{-1}$ spectral range.

Electrical and thermal transport properties of the 3, 5, and 10 h milled annealed and un-annealed (10 h milled) samples were studied in a Quantum Design Dynacool-9 physical properties measurement system (PPMS). For thermal and electrical contacts, four copper wires of 0.85 mm diameter were attached to each of the samples of rectangular shape with silver epoxy H20E and dried for 1 h in air. The contacts were further dried at 100°C (2°C/min heating rate) in the Ar atmosphere for 2 h. The samples with contacts were then mounted on the TTO (thermal transport option) port and incorporated into the PPMS system for electrical and thermal measurements. All the measurements were performed in the 30–400 K temperature range to study the temperature dependence of the transport behavior of the samples.

## 3. Method of analysis

Rietveld's refinement of XRD data is one of the most effective means for the structure and microstructure analysis of crystalline materials [44−46]. In the present study, we have utilized the Rietveld refinement software MAUD (version 2.55) [47] for analyzing XRD data of the annealed and unannealed $Sb_2Te_3$ nanostructures fabricated by mechanical alloying. A pseudo-Voigt (pV) analytical function was considered to estimate the individual contribution of size and lattice strain in the fitting of experimental peak broadening [48,49]. A specially prepared Si standard [50] was used for eliminating the instrumental broadening effect on the acquired sample data. A polynomial of degree 6 has been considered for fitting the background intensity of each XRD pattern. The Marquardt least-squares method was adopted for minimization of the difference between the observed ($I_O$) and simulated/calculated ($I_C$) intensities of the XRD patterns. The quality of fitting expressed as the goodness of fit (GoF) was defined as:

$$GoF = R_{wp}/R_{exp} \tag{1}$$

where $R_{wp}$ and $R_{exp}$ are the weighted residual error and expected error, respectively [47,50,51]. Refinements through iterative processes were continued until the GoF value approaches close to unity, which indicates the convergence between experimental and refined data. In all the cases, the GoF value varied between 1.06 and 1.09, indicates good fitting between the experimental and simulated data.

## 4. Results and discussion

### 4.1. Structure and microstructure characterization

XRD patterns of an unmilled Sb + Te powder mixture and as-grown samples prepared by 1, 3, 5, and 10 h ball-milling are presented in Fig. 1. As can be noticed, the diffraction pattern of the

unmilled powder mixture (0 h milling) revealed all significant reflections, exclusively from the elemental Sb (space group: R-3m) and Te (space group: $P3_121$). While the peaks matched well with corresponding standard diffraction patterns of the elements (Sb: JCPDS # 35−0732, Te: JCPDS# 36-1452), relative intensities of all the reflections are also in good agreement with the corresponding phase abundance in the mixture. It can also be noticed (Fig. 1) that the formation of the $Sb_2Te_3$ phase was initiated after 1 h of ball milling and completed after 3 h of milling. There is no significant difference between the XRD patterns of 5 h and 10 h milled samples except an increase of peak broadening, probably associated to a reduction of crystallite size due to prolonged milling. All the prominent peaks of these diffraction patterns could be indexed to the standard diffraction planes of the $Sb_2Te_3$ phase (JCPDS file #15-0874). The results indicate the formation of pure nanocrystalline $Sb_2Te_3$ without contamination either from the precursors or from the milling medium. Apart from smaller crystallite size, observed broadening of the diffraction peaks might also be due to the accumulation of r.m.s. lattice strain, deformation, and twin stacking faults within the crystallites during ball milling [52].

As the structural and microstructural parameters play significant roles in the physical properties of nanostructured materials, we have analyzed the microstructural parameters of the fabricated nanostructures through Rietveld refinement of their XRD patterns. The experimental and refined simulated XRD patterns of the $Sb_2Te_3$ samples prepared by 3, 5, and 10 h ball milling after annealing are shown in Fig. 2(a). For highlighting the effect of thermal treatment, the Rietveld refinements of XRD data of the fresh and thermally annealed 10 h milled sample have been presented in Fig. 2(b). In both figures, solid red dots, continuous black, and blue lines represent experimental or observed (Io) XRD data, simulated or calculated (Ic) XRD patterns, and the residual (Io−Ic) intensity (plotted below the respective XRD pattern) respectively. As can be noticed, the 0 h milled sample revealed both antimony and tellurium phases. The single-phase rhombohedral $Sb_2Te_3$ (with hexagonal setting) was formed entirely after 3 h milling and structurally



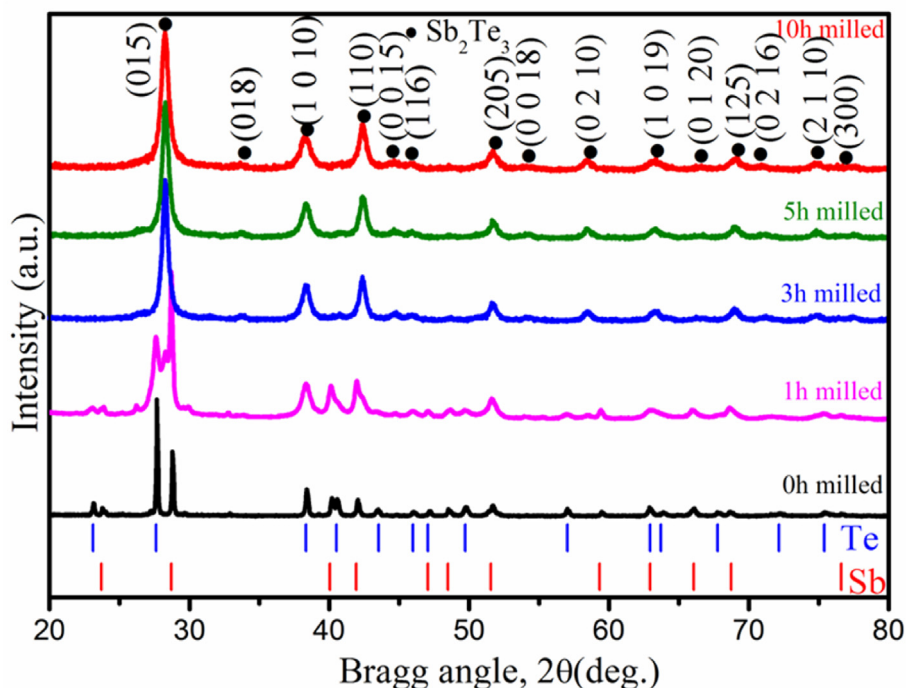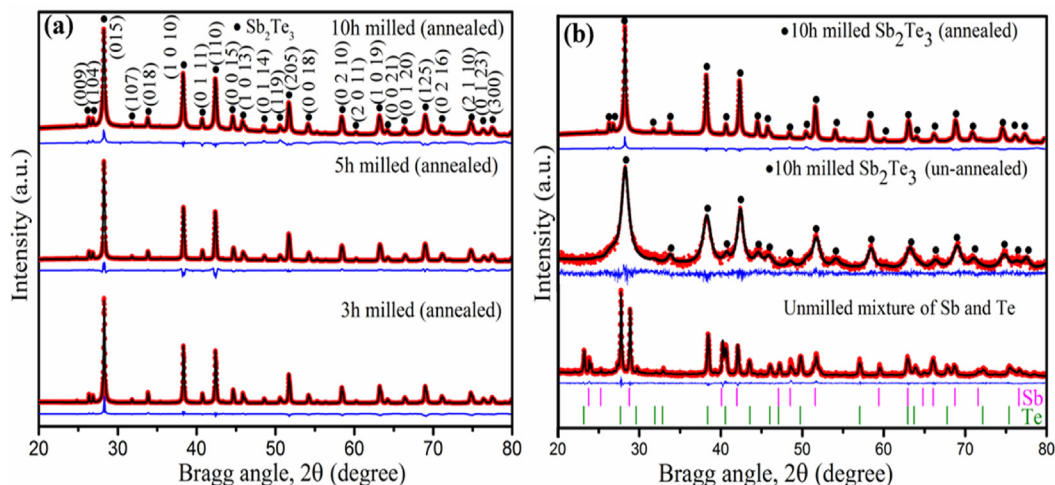**Fig. 1.** XRD patterns of the unmilled Sb + Te powder mixture (0 h milled) and $Sb_2Te_3$ samples prepared by 3, 5, and 10 h of ball milling.

**Fig. 2.** The Rietveld refinement output of (**a**) all the ball-milled samples after annealing, and (**b**) 10 h milled $Sb_2Te_3$ sample before and after thermal annealing, for comparison, the XRD pattern of the 0 h milled Sb + Te powder mixture, along with its Rietveld fitting has been included.

remained unaltered up to 10 h of milling. Thermal annealing in Ar atmosphere (Fig. 2(b)) induced no structural change, except a sharp increase in intensity and narrowing of diffraction bands. All the diffraction peaks of the 3, 5, and 10 h annealed samples (Fig. 2(a)) correspond to $Sb_2Te_3$ phase and are indexed as per JCPDS file #15-0874. Here all three experimentally obtained XRD patterns are fitted with $Sb_2Te_3$ (COD# 9007590, Sp. Group: R-3m(H), a = 4.264 Å, c = 30.458 Å) phase.

As can be seen in Fig. 2(a), residual intensity patterns for all the annealed samples are almost straight lines, indicating a good quality of fitting. As evident in Fig. 2(a), the peak-broadening increases gradually with milling time, probably due to the decrease of crystallite size on prolonged milling. While the XRD pattern of the 0 h milled sample (Sb + Te powder mixture) (Fig. 2(b)) could be simulated perfectly with elemental Sb (COD# 8100523,Sp. Group: R-3m (H), a = 4.2687 Å, c = 10.9244 Å) and Te (COD# 1011098, Sp. Group: $P3_121$, a = 4.454 Å, c = 5.924 Å) phases, the XRD patterns of the 10 h milled (annealed and unannealed) sample could be fitted with single $Sb_2Te_3$ phase (COD# 9007590, Sp. Group: R-3m(H), a = 4.264 Å, c = 30.458 Å). All major reflections of both 10 h milled un-annealed and annealed samples are identified and indicated with solid dot symbols (Fig. 2(b)). Enhanced sharpness of XRD peaks of the annealed samples is associated with increases in crystallite size, along with a reduction of lattice strain in the nanocrystals due to thermal treatment. Some weak intensity peaks, which are absent in the milled pattern due to size broadening, became visible after annealing. Structural and microstructural parameters obtained by Rietveld refinement of the 10 h milled $Sb_2Te_3$ sample before and after its thermal treatment are presented in Table 1. As can be seen, there is a significant increase in crystallite size and reduction of lattice strain after annealing the sample. However, lattice parameters remained almost unchanged on thermal annealing of the sample.

Fig. 3 shows the variation of crystallite size as well as r.m.s. lattice strain with milling time for the annealed samples. The average crystallite size of the annealed samples diminished gradually from 300 nm to 125.15 nm as milling duration increased from 3 h to 10 h due to induced lattice deformation caused by mechanical alloying for a more extended period. However, the lattice strain increased insignificantly from ~ $4.10 \times 10^{-4}$ to $4.29 \times 10^{-4}$ in the nanocrystals due to inclusions of lattice imperfections caused by severe plastic deformation on the course of milling.

Fig. 4 shows the size and r.m.s. strain distributions in the Ar annealed $Sb_2Te_3$ nanocrystals as obtained from Rietveld analysis. As can be seen in Fig. 4(a), the crystallite

size distribution gradually becomes narrower with a shift of most probable size value towards lower value (~125 nm) with increasing milling time, indicating a reduction of crystallite size along with the formation of mono-dispersed nanocrystals due to prolonged mechanical alloying. On the other hand, the microstrain distributions (Fig. 4(b)) for all samples indicate that the lattice strain decreases asymptotically up to L ~125 nm and then became insignificant, which signifies that the nanocrystallites of sizes below 125 nm contain a significant quantity of strain.

Fig. 5 depicts the variation of lattice parameter with milling time for the annealed $Sb_2Te_3$ samples. The lattice parameter 'a' reduces, and 'c' increases with increasing milling time, indicating the crystallites are elongated gradually along its needle axis 'c' with increasing milling time.

Crystallinity and microstructure of the fabricated $Sb_2Te_3$ nanostructures were studied further by transmission electron microscopy (TEM). Fig. 6(a) shows a typical TEM image of the as-prepared $Sb_2Te_3$ sample prepared by 10 h of ball-milling. The formation of quasi-spherical particles of nanometer dimension (marked by isolated red circles) in the sample is evident in the TEM micrograph. As can be noticed in the size distribution histogram presented in
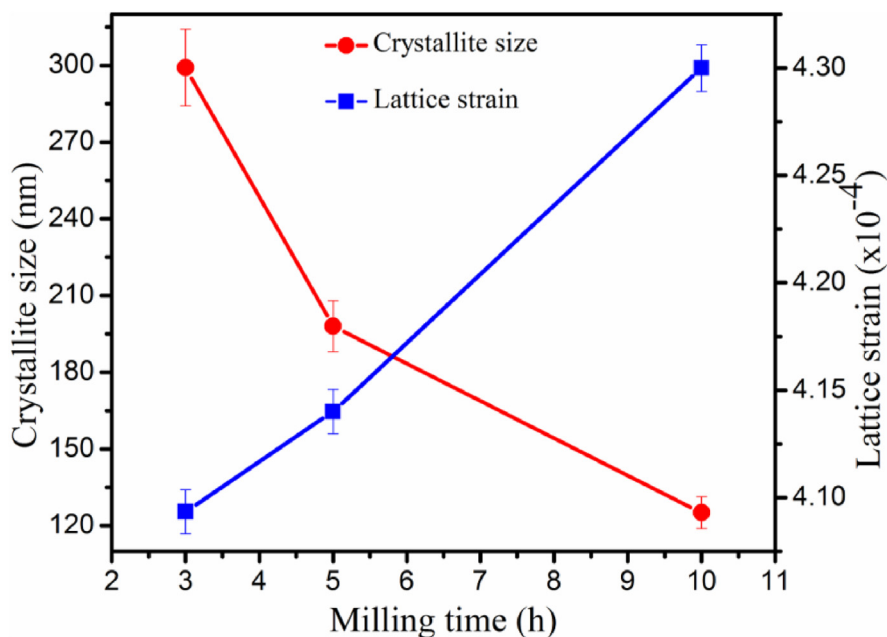
**Table 1**
Results of Rietveld refinement for 10 h milled $Sb_2Te_3$ sample before and after thermal annealing.

| Structural parameters | | 10 h milled un-annealed sample | 10 h milled annealed sample |
|---|---|---|---|
| Crystallite size (nm) $\pm$ ($10^{-2}$) | | 16.18 | 125.15 |
| Lattice strain $\pm$ ($10^{-5}$) | | $2.15 \times 10^{-3}$ | $4.29 \times 10^{-4}$ |
| Lattice parameters(Å) $\pm$ ($10^{-5}$) | a = b | 4.2644 | 4.2646 |
| | c | 30.4784 | 30.4784 |

**Fig. 3.** Variations of crystallite size and lattice strain with milling time for the thermally treated $Sb_2Te_3$ samples.
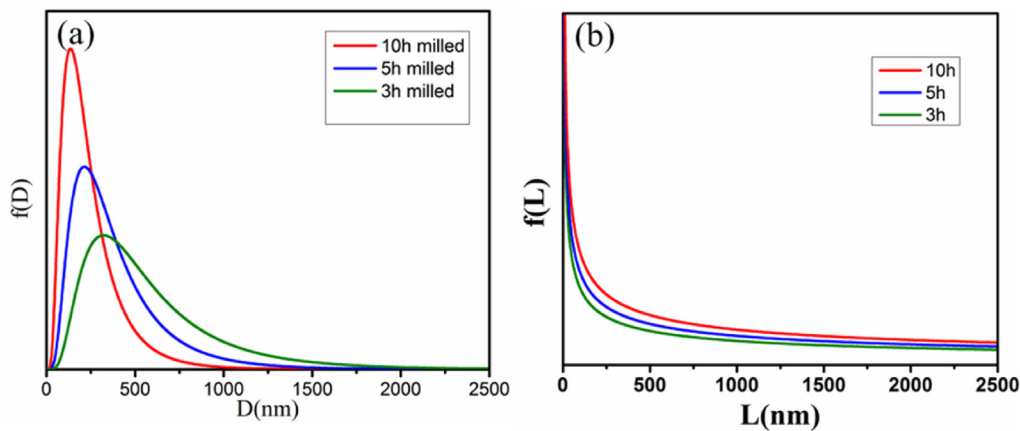


**Fig. 4.** Distributions of **(a)** crystallite size and **(b)** lattice strain among the crystallites in annealed $Sb_2Te_3$ samples.
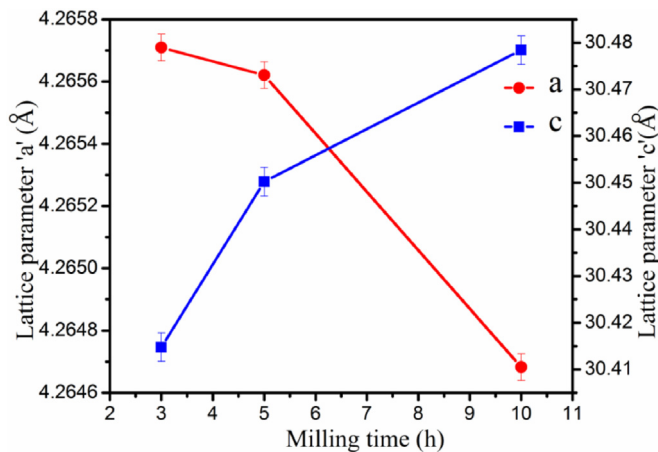


**Fig. 5.** Dependences of lattice parameters "a" and "c" on milling time in the annealed $Sb_2Te_3$ samples.

Fig. 6(b), the sample contains nanoparticles of narrow size dispersion (13-20 nm) with an average size ~ 17 nm. The selected area electron diffraction (SAED) pattern of the sample (Fig. 6(c)) revealed both continuous rings and well-defined diffraction spots, indicating the coexistence of nanostructured domains and coarser crystallites respectively after 10 h ball-milling. The appearance of multiple diffraction rings corresponds to different crystal planes that show the polycrystalline nature of the nanoparticles.

A significant grain growth could be noticed in the TEM image of the sample after thermal annealing (Fig. 6(d)). However, the particles become more disperse after thermal annealing, with size variation from 60 to 180 nm. The average size of the particles remained ~120 nm (Fig. 5(e)), which is about seven times bigger than the particle size in the sample before its thermal annealing. The SAED pattern of the sample (10 h milling, annealed) presented in Fig. 6(f) revealed its much-improved crystallinity, with high contrast and well-defined diffraction rings containing sharp diffraction spots. All the diffraction rings of the samples (annealed and un-annealed) could be assigned to the lattice planes of $Sb_2Te_3$.
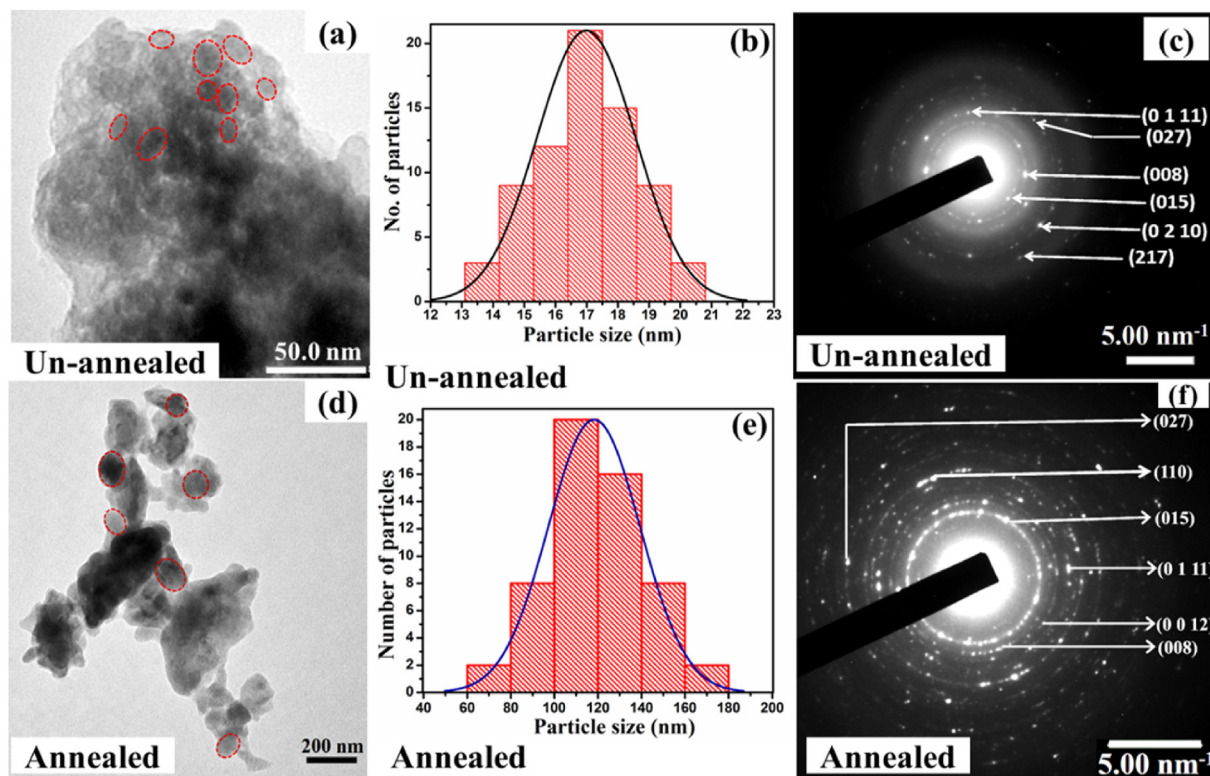
**Fig. 6.** a) TEM image, (b) grain size distribution histogram, and (c) indexed SAED pattern of as-grown (unannealed) $Sb_2Te_3$ nanoparticles prepared by 10 h ball milling. (d) TEM image, (e) grain size distribution histogram, and (f) indexed SAED pattern of annealed $Sb_2Te_3$ nanoparticles prepared by 10 h ball milling.

The absence of unidentified diffraction rings in the diffraction pattern of the samples indicates the lack of any other phase or impurity in the nanostructures, in complete agreement with the results obtained from the Rietveld refinement of their XRD patterns.

Fig. 7 presents typical SEM images and particle size distribution histograms of the as-grown and thermally annealed $Sb_2Te_3$

particles fabricated by 10 h ball milling. Effects of thermal annealing on grain-growth, enhancement of particle size, along with compactness of the particle-matrix are clear from these images. Due to annealing, the spherical-shaped nanoparticles (Fig. 7(b)) grow inhomogeneously along different planes, producing faceted particles of anisotropic shapes (Fig. 7(e)). In contrast, the size distribution of the particles in both the as-grown and annealed
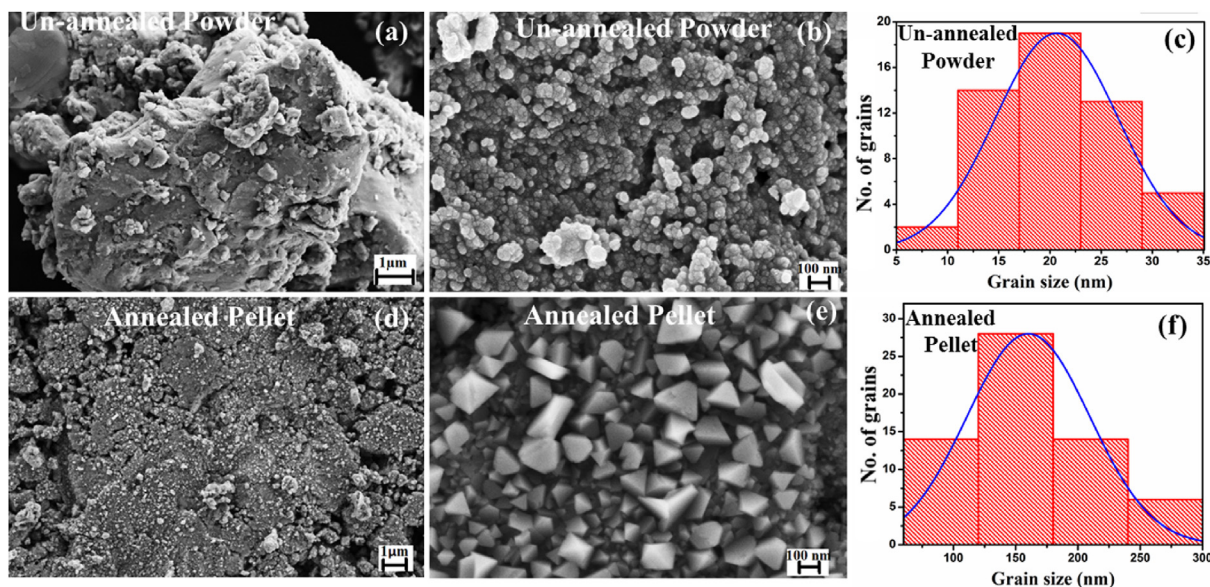


**Fig. 7.** Typical **(a,b)** SEM images and **(c)** size distribution histogram of the as-grown $Sb_2Te_3$ particles prepared by 10 h ball milling. Representative **(d,e)** SEM images and **(f)** size distribution histogram of the annealed $Sb_2Te_3$ particles prepared by 10 h ball milling.

samples could be fitted well with Gaussian distribution (Fig. 7(c),(f)). The average size of the particles increased from ~20 nm to ~150 nm due to thermal annealing, which is close to the corresponding values estimated both from the Rietveld refinement and TEM analysis of the samples (Fig. 6).

For analyzing the effect of thermal treatment, the qualitative energy dispersive X-ray (EDX) analysis was performed on the as-grown and annealed $Sb_2Te_3$ nanostructures prepared by 10 h ball milling, and the results are shown in Fig. 8(a) and (b), respectively. The EDX spectrum of the sample (Fig. 8(a) and (b)) revealed characteristic emission bands of Sb and Te, along with C originating from carbon tape utilized for sample mounting. There appeared no signal correspond to any other element in the EDX spectrum of the sample, indicating the high purity of the fabricated nanostructures. The EDX estimated elemental composition of the as-grown (unannealed) nanostructures (Fig. 8(a)) was ~40.33 at% Sb and ~59.67 at% Te, which is close to the stoichiometry of the compound $Sb_2Te_3$. On the other hand, the thermally annealed nanostructures also revealed Sb and Te distribution with 39.11 and 60.89 at% Sb and Te contents (Fig. 8(b)), respectively. The results demonstrate that the mechanical alloying process with subsequent thermal annealing utilized in the present study is very useful for fabricating stoichiometric $Sb_2Te_3$ nanostructures of high crystallinity without significant contamination from the reaction medium.

Considering the structure and microstructural parameters obtained from the Rietveld refinement of XRD pattern of the $Sb_2Te_3$ nanostructures prepared by 10 h ball milling (annealed), an atomic model of the $Sb_2Te_3$ lattice could be constructed and presented in Fig. 9. Positions of Sb and Te atoms in the rhombohedral (hexagonal) unit cell are shown along with the a, b, and c axes directions. Locations of the densest lattice planes (0 1 5) in the unit cell are shown in cyan color, along with their interplanar spacing ($d_{015}$).

### 4.2. FTIR spectra and bandgap estimation of the $Sb_2Te_3$ nanoparticles

Fig. 10 depicts the FTIR transmission spectra of the 10 h milled sample before and after thermal annealing, recorded over 400-4000 $cm^{-1}$ spectral range. Both the samples revealed 6 clear absorption bands in their FTIR spectrum, which could be identified. The absorption band appeared around 734 $cm^{-1}$ for both the samples corresponds to the Sb—O—Sb stretching vibration [53], which may occur due to surface oxidization. The absorption peak becomes prominent after annealing. It may happen due to the presence of oxygen as leakage during Ar annealing and the more chances of surface oxidization than the unannealed one. The band revealed at 1635 $cm^{-1}$ corresponds to the C=O stretching mode of absorbed $CO_2$ [54,55], and the 2351 $cm^{-1}$ band corresponds to —C-H bond [55] of the organic molecules absorbed during the sample preparation and handling. The broadband appeared around 3410 $cm^{-1}$ is attributed to the hydroxyl (-OH) group of water adsorbed at the surface of the powder sample [54,55]. As can be noticed, the absorption band is considerably broader and intense for the as-grown (unannealed) sample in comparison to the annealed sample due to the reduction of adsorbed water on thermal annealing. The absorption bands appeared at ~3782 $cm^{-1}$, and ~3892 $cm^{-1}$ correspond to free —OH stretching vibrations [56,57].
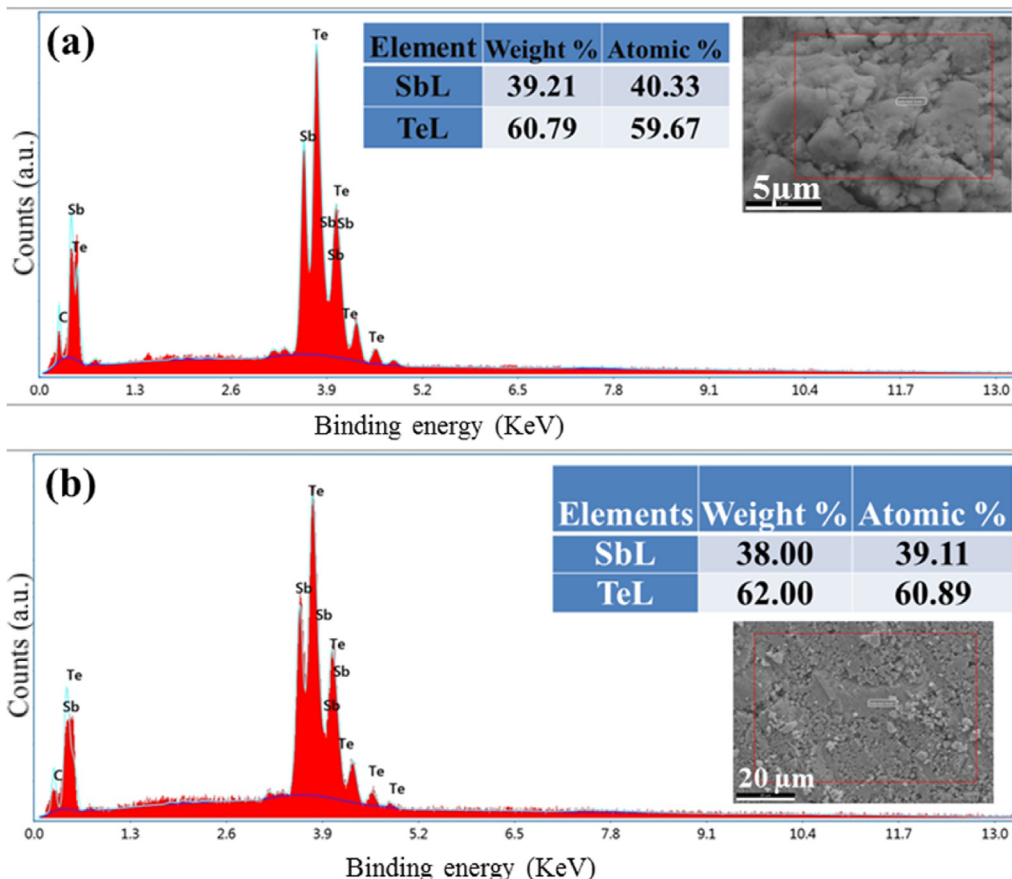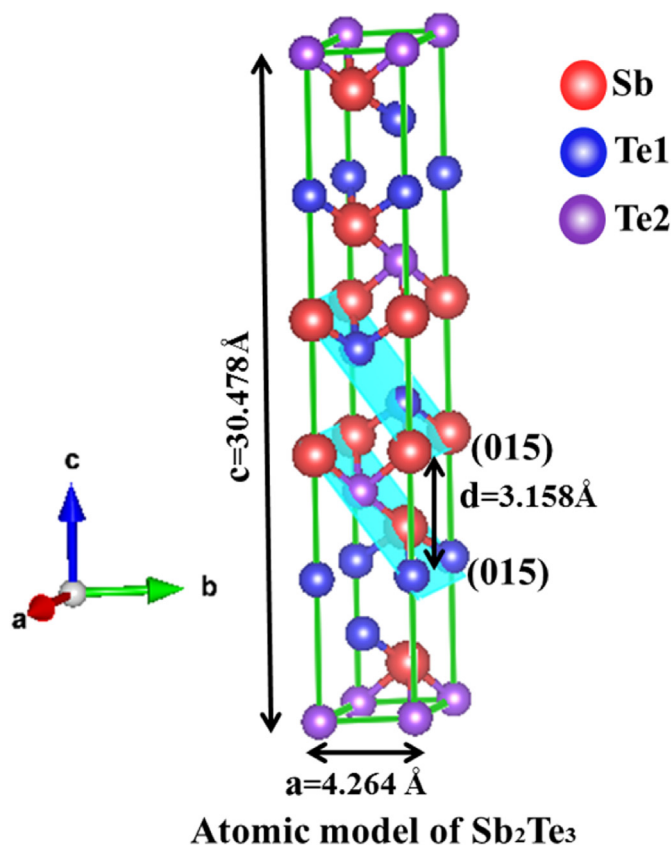


**Fig. 8.** EDX spectrum (inset showing corresponding weight % and atomic %) of **(a)** the 10 h milled un-annealed $Sb_2Te_3$ sample, **(b)** the 10 h milled annealed $Sb_2Te_3$ sample.

S. Paul, U. Pal and S.K. Pradhan

**Fig. 9.** Atomic model of the rhombohedral (hexagonal) $Sb_2Te_3$ lattice constructed using the microstructural parameters obtained by Rietveld refinement of XRD pattern of the sample prepared by 10 h ball milling and annealing.
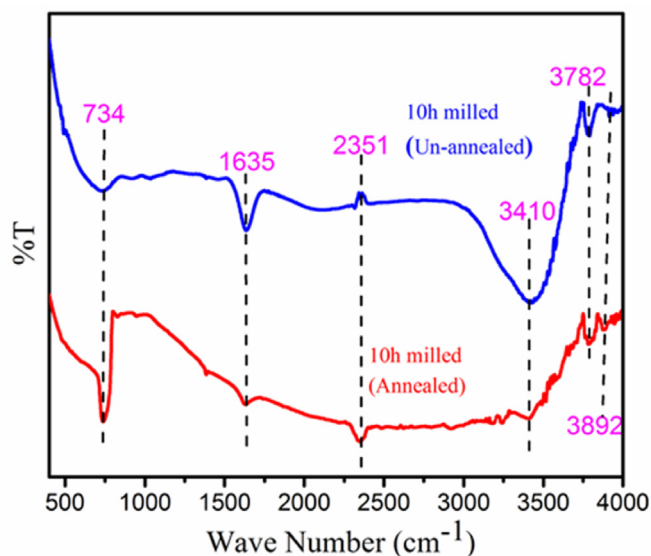


**Fig. 10.** FTIR transmission spectra of the 10 h milled $Sb_2Te_3$ sample, before (blue) and after (red) thermal annealing in Ar atmosphere. (For interpretation of the references to color in this figure legend, the reader is referred to the Web version of this article.)

For determining the bandgap energy of the fabricated $Sb_2Te_3$ nanostructures and the effect of thermal annealing on it, we have analyzed the nanostructures fabricated by 10 h ball milling. For that, the optical absorption coefficients ($\alpha$) of the as-grown and annealed samples were determined at each wavelength/wavenumber from the measured transmission data using the relation [54,55,58]:

$$\alpha = \frac{1}{t} \, ln \frac{1}{T} \tag{2}$$

where $t$ and $T$ are the thickness of the pellet sample and transmittance, respectively. The optical band gaps ($E_g$) of the unannealed and annealed samples are obtained using the Tauc relation [54,55,58]:

$$\alpha h\nu = A(h\nu - E_g)^n \tag{3}$$

where $A$ is a constant and the exponent $n$ can have different values (1/2, 2, 3/2, 3) depending upon the type of transitions (allowed direct, allowed indirect, forbidden direct, forbidden indirect transition), respectively. The value of $n = 1/2$ was considered for $Sb_2Te_3$ as the optical transition is a direct allowed transition. The bandgap was calculated from the Tauc plot by extrapolating the straight-line portion of the curve to the horizontal axis with $\alpha h\nu = 0$.

Fig. 11 shows the Tauc plots of 10 h milled $Sb_2Te_3$ nanoparticles before and after thermal annealing in Ar atmosphere. The bandgap values estimated from the Tauc plots of the samples were 0.32 and 0.15 eV, respectively (Fig. 11 (a) and (b)). The bandgap energy estimated for the as-grown (unannealed) $Sb_2Te_3$ nanostructures is quite comparable to the bandgap energy of the narrow bandgap semiconductor reported in the literature (~0.3 eV) [21,59]. However, the bandgap energy decreased considerably after the thermal treatment of the nanostructures, probably due to highly increased grain growth. The bandgap energy estimated for our thermally annealed sample (0.15 eV) is close to the energy gap value of hot-pressed $Sb_2Te_3$ (~0.16 eV) reported by Hu et al. [60].

### 4.3. Thermo-electric characterizations of the $Sb_2Te_3$ sample

#### 4.3.1. Electrical resistivity

The temperature dependence of electrical resistivity of the annealed samples (3, 5, and 10 h milled) measured in 30−400 K temperature range is shown in Fig.12(a). As can be seen, the electrical resistivity of all the annealed samples is increased quasi-linearly with the increase of temperature, manifesting their metallic or degenerate semiconducting behaviors. It is clear from the figure that the grain size plays a vital role in electrical property. With reducing grain size, the value of resistivity increases due to a rise in the grain boundary scattering of the charge carriers. As a result of this, electrical conductivity reduces as milling time increases from 3 h to 10 h.

The effect of annealing on the resistivity of the 10 h milled sample, before and after annealing, is presented in Fig. 12(b). As can be noticed, the electrical resistivity of the as-prepared (unannealed) nanostructures is decreased with the increase of temperature, as expected for a semiconducting material. However, after thermal annealing, the nanostructures reveal the characteristics of the metal or degenerate semiconductor, i.e., the resistivity increased with the increase of temperature. As the elemental composition of the nanostructures did not change much due to thermal annealing at 300 °C (insets of Fig. 8), the metallic or degenerate semiconducting behavior of the annealed sample can be associated to its reduced bandgap energy (Fig. 11), which we associated to the grain growth due to thermal annealing (confirmed in microstructural analysis). The thermal annealing performed on the compressed (pelleted) nanostructures not only induces a grain growth but also enhances their compactness (see the FESEM images in Fig. 7(d)&(e)). As the porosity plays a vital role in the electric
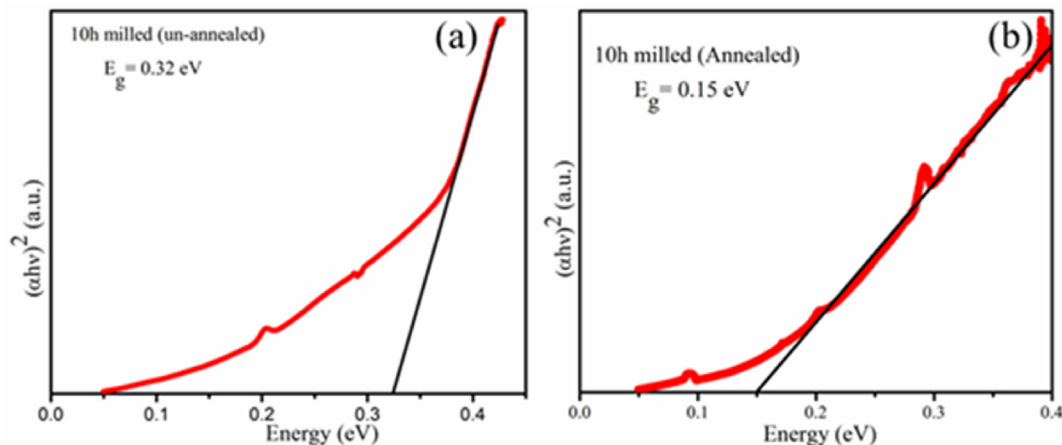
*S. Paul, U. Pal and S.K. Pradhan*

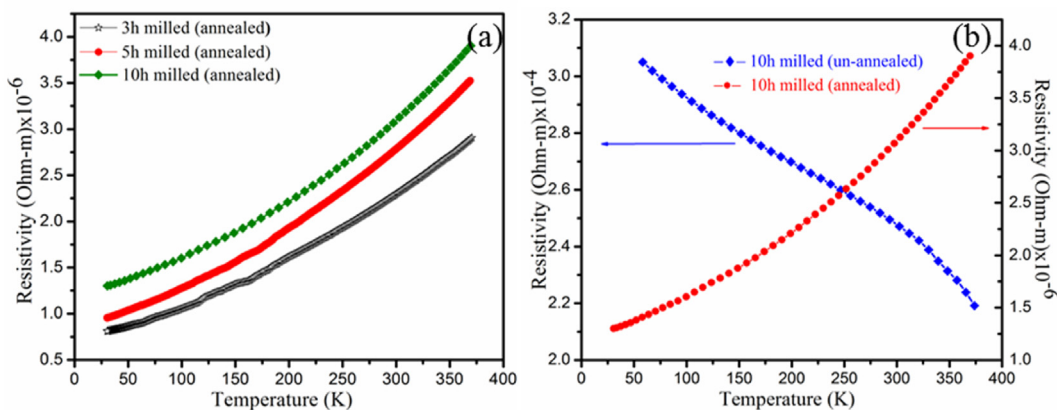**Fig. 11.** Tauc plots of 10 h milled Sb$_2$Te$_3$ nanoparticles **(a)** before and **(b)** after thermal annealing.



**Fig. 12.** **(a)** Temperature variation of electrical resistivity for the annealed Sb$_2$Te$_3$ nanoparticles prepared using different milling times, and **(b)** temperature variation of resistivity of the as-grown and annealed Sb$_2$Te$_3$ nanoparticles prepared by 10 h ball milling.

transport properties [61], the resistivity of the annealed sample is considerably less (about two orders) than the unannealed sample. The room temperature (300 K) electrical conductivity of the annealed sample was ~3.2 × 10$^5$ mho/m, which is significantly higher than the previously reported room-temperature electrical conductivity values of Sb$_2$Te$_3$ nanostructures [16,19,26,39,62]. However, the conductivity of our 10 h milled annealed nanoparticles is comparable with the reported room-temperature electrical conductivity value of Sb$_2$Te$_3$ thin films prepared by metal-organic chemical vapor deposition [18].

### 4.3.2. Seebeck coefficient and power factor

Fig. 13(a) shows the variation of the Seebeck coefficient with temperature for the annealed Sb$_2$Te$_3$ nanoparticles prepared by ball milling for different durations, i.e., of different sizes. The positive values of the Seebeck coefficient of the samples indicate their p-type conductivity [63]. The Seebeck coefficient in all the samples increases with temperature. It is evident that initially, at the low-temperature zone, the Seebeck coefficient increases as milling time increases. The result can be explained as follows. For a metallic sample or a degenerate semiconductor (energy independent scattering approximation), the expression of the Seebeck coefficient can be expressed as [1]:

$$S = \frac{8\pi^2 K_B^2}{3eh^2} m^* \, T \left(\frac{\pi}{3n}\right)^{2/3} \tag{4}$$

where m* is the effective mass of the carriers, n is the carrier concentration, K$_B$ is the Boltzmann constant, and h is the Planck constant. The equation (4) indicates that the Seebeck coefficient is inversely proportional to the carrier concentration. With the increase of milling time, the increase of electrical resistivity (Fig. 12(a)) assures the reduction of carrier concentration. Hence an increase in the Seebeck coefficient occurs. However, with the increasing temperature, Seebeck coefficient values of 3 h and 5 h milled samples coincide, whereas that of 10 h milled sample gradually increases with a comparatively higher value than 3 h or 5 h milled samples. Fig. 13(b) shows the temperature dependence of the Seebeck coefficient for the 10 h milled sample before and after annealing. We can see that for a fixed temperature value, the Seebeck coefficient decreases after annealing. The drastic enhancement of electrical conductivity of the samples after thermal annealing (Fig. 12(b)) indicates a considerable increase of carrier concentration in them. As a result, the Seebeck coefficient of the sample at a specific measurement temperature decreases after thermal annealing. It is also seen that for both as-grown and annealed samples, the Seebeck coefficient increases with

*S. Paul, U. Pal and S.K. Pradhan*
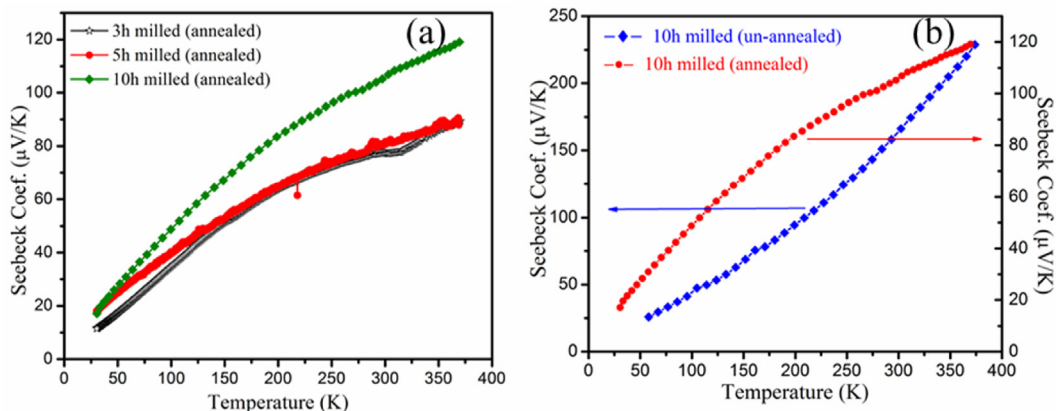
**Fig. 13. (a)** Temperature dependence of Seebeck coefficient for the annealed $Sb_2Te_3$ nanoparticles prepared at different milling times, and **(b)** temperature variation of Seebeck coefficient for the as-grown and annealed $Sb_2Te_3$ nanoparticles prepared by 10 h ball milling.

temperature, which can be related to the proportionality relation between the Seebeck coefficient and temperature (eq. (4)). Room temperature Seebeck coefficient value estimated for the 10 h milled annealed $Sb_2Te_3$ sample is comparable to the room temperature Seebeck coefficient values of chemical vapor deposited $Sb_2Te_3$ thin film [18] reported earlier.

From the experimentally obtained values of Seebeck coefficient (S) and electrical resistivity ($\rho$), the power factor ($S^2/\rho$) for the thermally annealed samples were calculated and plotted against temperature in Fig. 14(a). As can be seen in Fig. 14(a), the power factor increases with temperature for the whole range of measurement (40-380 K), mainly due to the positive slopes of the Seebeck coefficient vs. temperature curves. While the 10 h milled sample has the highest power factor, the power factor of the 5 h milled sample is lower than that of the 3 h milled sample below 120 K (Fig. 14(a)) due to its higher resistivity compared to the 3 h milled sample. Fig. 14(a) also shows a saturated behavior of power factor for all the annealed materials at a higher temperature (~200 K), and the highest value of power factor obtained for 10 h milled annealed material is ~37×10$^{-4}$ WK$^{-2}$m$^{-1}$. The effect of thermal annealing on the power factor of the $Sb_2Te_3$ nanostructures has been depicted in Fig. 14(b), taking the 10 h milled sample as a reference. As can be seen, the power factor of the sample increased from ~10$^{-5}$ to ~10$^{-4}$ unit after thermal annealing, which is basically due to the reduction of electrical resistivity of the sample after

annealing. The power factor value at room temperature for the 10 h milled annealed sample is ~36.361×10$^{-4}$ WK$^{-2}$m$^{-1}$, which is quite comparable to the power factor values of $Sb_2Te_3$ nanostructures, reported by Zakeri et al. [26], Morikawa et al. [33], and Fang et al. [39].

### 4.3.3. Thermal conductivity

Fig. 15 presents the temperature dependence of the thermal conductivity of the thermally annealed samples. The thermal conductivity of all the samples increased with temperature. Total thermal conductivity (K) of a crystalline semiconductor consists of (i) electronic thermal conductivity ($K_e$) and (ii) lattice thermal conductivity ($K_l$). The electronic thermal conductivity, $K_e$, which is the contribution of charge carriers, can be determined from the Wiedemann−Franz law: $K_e = \sigma L T$, where $\sigma$ is the electrical conductivity, T is the absolute temperature, and L is the Lorenz number with a value of $2.45 \times 10^{-8}$ W $\Omega/K^2$. Due to the higher kinetic energy of the charge carriers, electronic contribution in the total thermal conductivity is substantial at higher temperatures.

On the other hand, the lattice thermal conductivity is the contribution of phonons. At higher temperatures, two cases may occur: i) as temperature increases, the lattice vibration in the sample increases. Hence, the thermal resistance of the samples increases with a reduction of thermal conductivity; ii) with the increase of temperature, the grain sizes of the samples might also
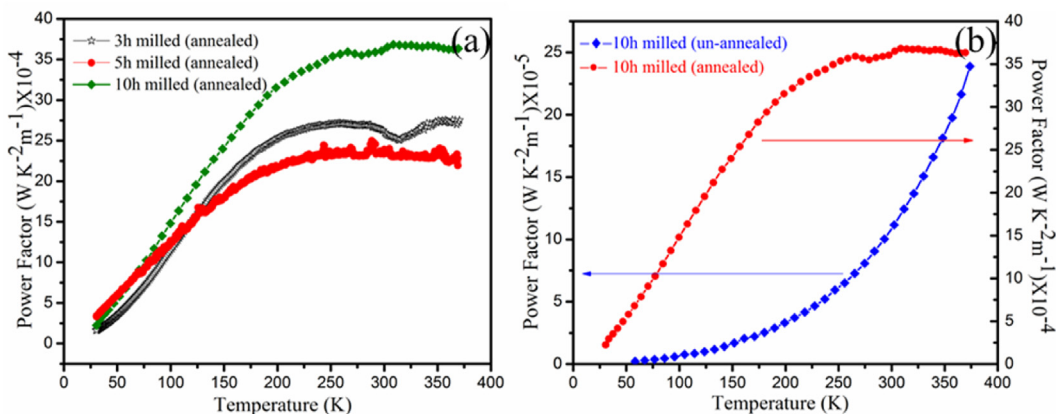


**Fig. 14. (a)** Temperature dependence of power factors for 3 h, 5 h, and 10 h milled, annealed samples, **(b)** Temperature dependence of power factor of 10 h milled sample before and after annealing.
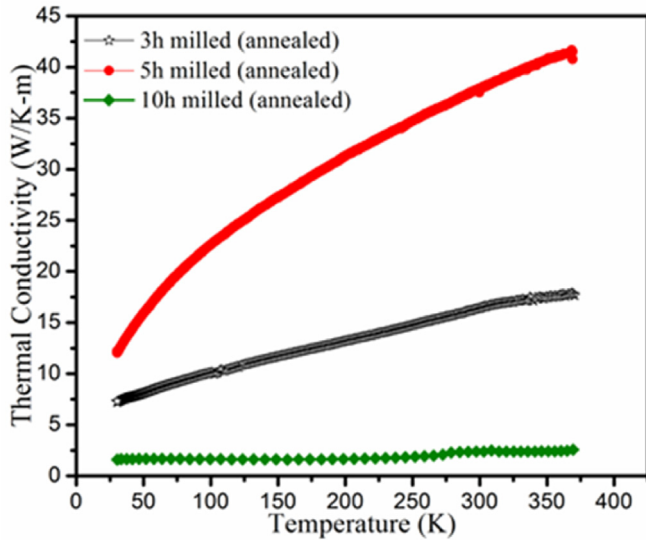
**Fig. 15.** Temperature variation of total thermal conductivity for 3 h, 5 h, and 10 h milled samples (annealed).



**Fig. 16.** The temperature dependencies of effective Lorentz number for 3, 5 and 10 h milled samples after annealing.

increase if the grain growth has not been completed during annealing. As a result, fewer phonons are scattered at the grain boundary, which increases thermal conductivity. In the present work, the lattice thermal conductivity is dominated by the second factor, and the electronic thermal conductivity increases with temperature. As a result, the total thermal conductivity increases with temperature. As can be noticed in Fig. 15, for a specific temperature, the total thermal conductivity is lowest for the 10 h milled sample; i.e., the sample with the smallest particle size. At the same time, both the 3 h and 5 h milled samples reveal thermal conductivity higher than the 10 h milled sample. The thermal conductivity of the 3 h milled sample is lower than that of the 5 h milled sample, although the former sample has a larger particle size than the latter. Such an anomaly in the thermal conductivity of the $Sb_2Te_3$ nanostructures could be explained considering the contribution of lattice thermal conductivity, as discussed later.

Let us now discuss the particle size and temperature dependence of electronic thermal conductivity ($K_e$) and lattice thermal conductivity ($K_l$) separately. The lattice thermal conductivity value of the 10 h milled sample becomes negative in some temperature range if we calculate the electronic thermal conductivity from Wiedemann−Franz law ($K_e = \sigma LT$) using a constant value of Lorenz number, $L = 2.45 \times 10^{-8}$ W $\Omega/K^2$ (degenerate limit). This result is not practical and appeared because of the incompleteness in the value of the Lorenz number. Actually, Lorenz number is not a constant but depends on the scattering mechanism, carrier concentration, and Fermi energy [64]. Since $Sb_2Te_3$ is a narrow and direct bandgap semiconductor, it can be described by the non-parabolic band model [65]. The most appropriate model in this context is the Kane model [66]. For narrow bandgap semiconductors, due to powerful interaction between the valence band and conduction bands, the parabolic nature of the band is distorted. Hence, L value deviates from the equation as proposed by Kim et al. considering a single parabolic band (SPB) model with an acoustic phonon scattering (APS) [67]. For single Kane band (non-parabolic) assuming APS, the Lorenz number (L) and Seebeck coefficient (S) are not only functions of the reduced Fermi energy ($\eta$) (as for the case of SPB with APS), but also functions of the non-parabolicity parameter ($\alpha = K_BT/E_g$, $E_g$ the band gap) [67]. From the Boltzmann equation and non-parabolic Kane band model for the energy
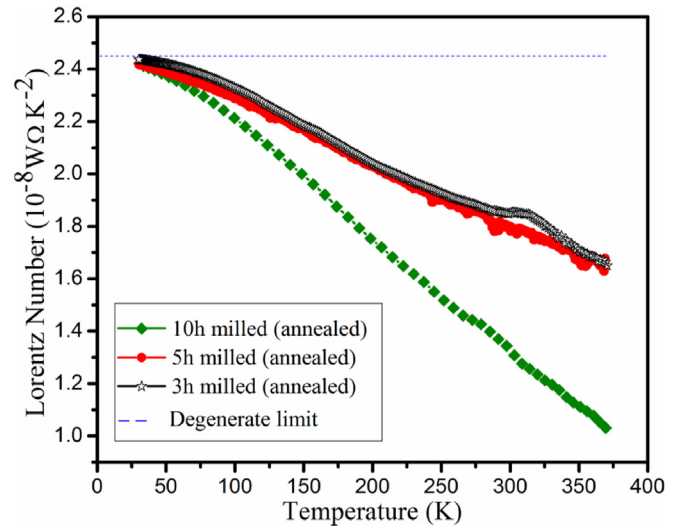
dispersion, the total thermal conductivity K can be obtained as,

$$K = K_l + K_{el,J} \tag{5}$$

$$K = K_l + K_{el,E} - T\sigma S^2 \tag{6}$$

where $K_l$ is the lattice contribution, $K_{el,J}$ is the electronic contribution at constant current and $K_{el,E}$ is the electronic contribution at constant electric field [65,68]. For metals (with small S) or semiconductors with small carrier concentration (hence small $\sigma$), the quantity $T\sigma S^2$ is almost negligible, indicating $K_{el,J} \approx K_{el,E}$. However, in good thermoelectric material, $T\sigma S^2$ has a significant value, and both above the thermal conductivities differ from each other.

Now according to Wiedemann-Franz law, $K_{el,E} = L_0\sigma T$, with $L_0 = 2.45 \times 10^{-8}$ W$\Omega/K^2$, the effective Lorentz number can be defined as, $L_{effective} = K_{el,J}/\sigma T$ [69]. Temperature variations of effective Lorenz number for all the annealed $Sb_2Te_3$ samples in the present work are shown in Fig. 16. From the figure, it is clear that the effective value of L is smaller than that of the constant value at the degenerate limit (indicated by the blue dashed line in Fig. 16). The effective Lorentz number decreases as temperature increases and particle size decreases. Using the L value (as obtained from the curve in Fig. 16), the electronic thermal conductivity and the lattice thermal conductivity are calculated for the annealed samples prepared by different durations of ball milling and plotted against temperature in Fig. 17.

As can be noticed in Fig. 17(a), for a specific temperature, the electronic thermal conductivity decreases with particle size reduction because of the decrease in both the electrical conductivity($\sigma$) and the effective Lorentz number with reducing particle size. From Fig. 17(b), it is seen that lattice thermal conductivity shows similar nature as the total thermal conductivity. As temperature increases, the lattice thermal conductivity of all samples increases because of the occurred grain growth dominating over the thermal vibrations, as discussed before in the case of total thermal conductivity. Alternatively, if the activation of minority carriers with temperature is ignored, then the relation of lattice thermal conductivity and 1/T should be linear [70], indicating $K_l$ should have decreased with increasing temperature. However, the opposite characteristic is noticed, which is attributed to the subscription of minority carrier (bipolar effect) to $K_l$ value [71−76]. The
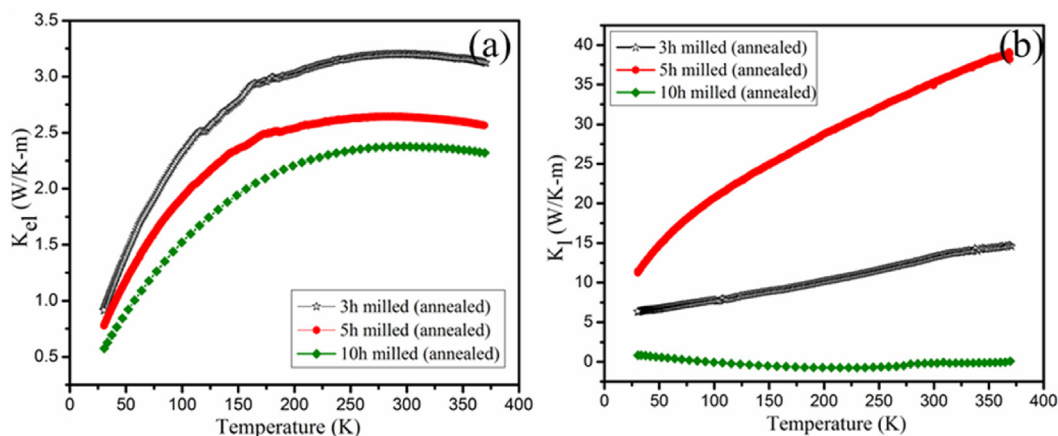
**Fig. 17.** Temperature dependence of **(a)** electronic thermal conductivity and **(b)** lattice thermal conductivity for the $Sb_2Te_3$ samples prepared by 3, 5, and 10 h ball milling and annealing.

value of $K_l$ is the smallest for the 10 h milled sample because of its smallest grain size. Because of comparatively larger grain size, the 3 h milled and 5 h milled samples show relatively larger $K_l$. The grain size and lattice strain have essential roles in controlling the lattice thermal conductivity of nanostructures [77,78]. The thermal conductivity of a spherical nano solid can be described as [77],

$$K_p = K_b \left(1 - \frac{2d}{D}\right)^{\frac{3}{2}} \tag{7}$$

where $K_p$ and $K_b$ are respectively the thermal conductivities of the spherical nano solids and the bulk materials, D and d respectively represent the diameter of the spherical nano solids and the diameter of the atoms of the nano solids. Hence, it is evident from Eq. (7) that there is a direct relationship between thermal conductivity and particle size of the nanocrystallites, mainly because of the phonon − grain boundary scattering effect. Here actually, the size reduction is associated with the enhanced phonon-boundary scattering. With reducing grain size, more numbers of phonons may scatter at the grain boundaries. As a result of this, lattice thermal conductivity tends to decrease. However, lattice strain has an inverse impact on thermal conductivity [78]. As the lattice strain increases by incorporating more defect densities in the samples, the phonon−impurity scattering increases, and hence thermal conductivity reduces. The Rietveld analysis reveals that the lattice strain increases with milling time. These two reasons clearly explain the thermal conductivity results of 5 h and 10 h milled $Sb_2Te_3$ samples. However, the 3 h milled sample shows unexpected results of $K_l$ and total thermal conductivity K. Although the 3 h milled sample has the largest grain size, it does not have the largest $K_l$ and the most significant K values. Whereas the 5 h milled sample with relatively smaller grain size and more substantial lattice strain has the most considerable $K_l$ value. It is because the phonon scattering from a solid is not only composed of phonon-grain boundary scattering and phonon-impurity scattering, but phonons may also scatter by the charge carriers [79]. If the carrier concentration is very high, then phonon-charge carriers scattering dominates over other mechanisms, and lattice thermal conductivity of the material is suppressed more [79]. In the case of 3 h milled sample, owing to higher carrier concentrations, more phonons are scattered due to predominating phonon-carrier scattering and hence reducing $K_l$ values below the values of the 5 h milled sample. Thus, the discrepancy in the results of lattice thermal conductivity and total thermal conductivity of the 3 h milled sample is resolved.

The temperature dependencies of the total thermal conductivity (K) for the 10 h milled sample before and after its thermal annealing are shown in Fig. 18. For both the unannealed and annealed samples, K increased with temperature. However, the thermal conductivity of the annealed sample remained higher than that of the unannealed sample, for the whole temperature range of measurement. Due to higher electrical conductivity, and hence a higher concentration of charge carriers, the contribution of electronic thermal conductivity of the annealed sample is higher than that in the unannealed sample. On the other hand, due to the bigger grain size in the annealed sample, grain boundary phonon scattering is low, which causes a higher lattice conductivity for the sample in comparison to the unannealed sample. Moreover, reduced lattice strain (Table 1) of the thermally annealed sample also contributes to its higher thermal conductivity [78]. The total thermal conductivity value for the 10 h milled sample annealed at 573 K (Fig. 18) is very close to the values reported by Park et al. [13] for their $Sb_2Te_3$ thin films after annealing at 573 K.

*4.3.4. Figure of merit*

The thermoelectric figure of merits of the $Sb_2Te_3$ nanostructures fabricated at different milling times and annealed at 573 K is measured in the 30-400 K temperature range and are presented in Fig. 19(a). As can be noticed, while the figure of merits of all three samples are very similar at low temperature (e.g., 26 K), the higher temperature figure of merit values of 10 h milled sample is substantially higher than that of the samples prepared by 3 h and 5 h of ball milling. For the 10 h milled annealed sample, the highest Seebeck coefficient value, and the lowest thermal conductivity tends to increase the value of ZT. Although its highest electrical resistivity value counteracts the increase of ZT, the contributions of S and K dominates. While comparing the values with 5 h and 3 h milled samples, it is noticed that the impact of thermal conductivity on the more considerable value of ZT is much more dominating. So the drastic increase in ZT value for 10 h milled sample (annealed) is mainly due to its lowest thermal conductivity value. Since the thermal conductivity of 5 h milled sample is the largest, its ZT value is lowest. Here the room temperature (300 K) ZT value is obtained as 0.468, and the maximum value of ZT within the measurable temperature range (~30 K−400 K) is 0.543 at 365 K for thermally treated 10 h milled sample.

Fig. 19(b) shows the ZT vs temperature curves of the 10 h milled sample before and after its thermal annealing. It should be noticed that the ZT value of the sample is increased by an order after
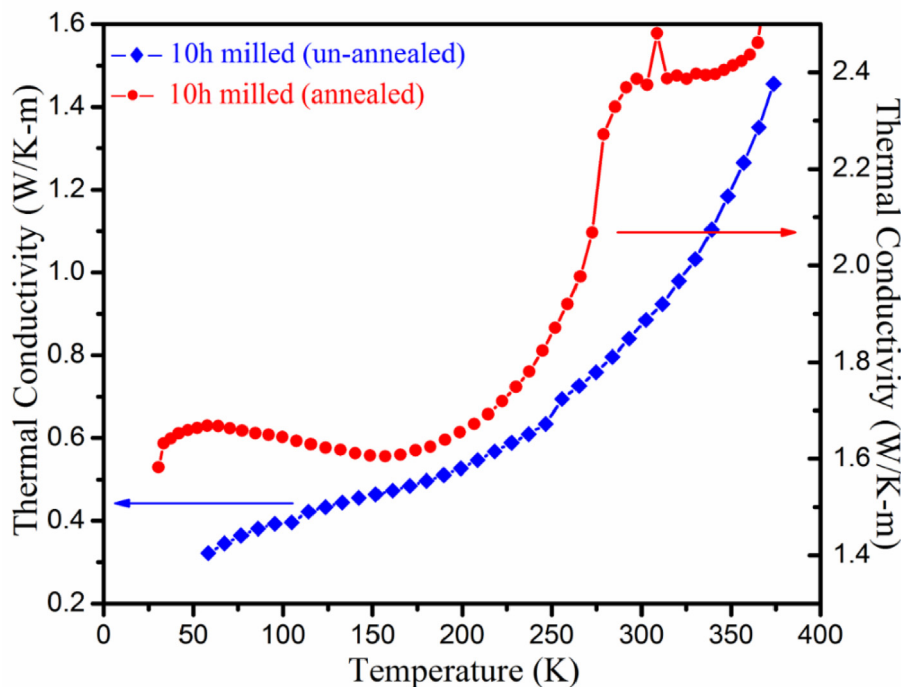
*S. Paul, U. Pal and S.K. Pradhan*

**Fig. 18.** Temperature variation of total thermal conductivity of the 10 h milled $Sb_2Te_3$ sample before and after annealing treatment.
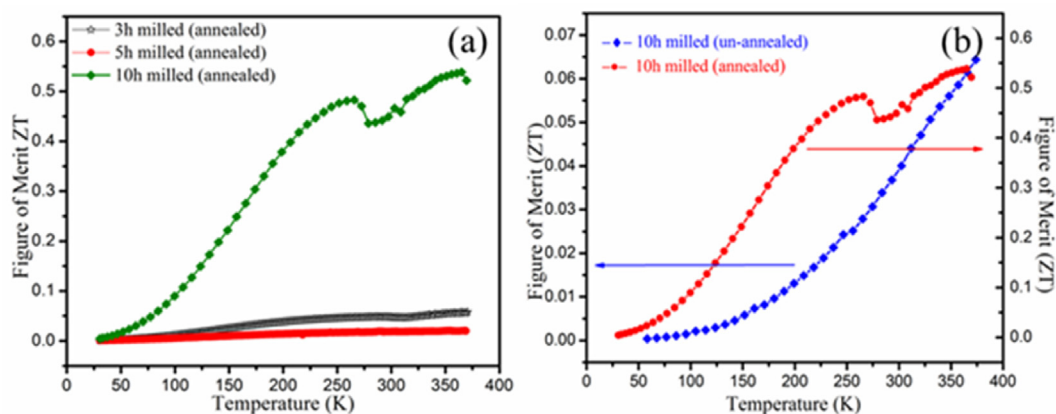


**Fig. 19.** (a) Temperature dependence of ZT for the annealed $Sb_2Te_3$ nanoparticles prepared by different milling durations, and (b) temperature dependences of ZT for the 10 h milled sample before and after annealing.

thermal annealing, probably due to the substantial increase in electrical conductivity. The room temperature ZT value increased from 0.039 to 0.468 due to heat treatment. The obtained room temperature ZT value for annealed $Sb_2Te_3$ nanostructures is slightly lower than the ZT value of $Sb_2Te_3$ nanoparticles, as obtained by Heimann et al. [24] fabricated by a relatively complicated synthesis process (microwave-assisted decomposition of the single-source precursor). It is comparable to the ZT values of $Sb_2Te_3$ nano-material reported by Goncalves et al. (ZT ~ 0.26) [62], Zou et al. (ZT ~ 0.56) [19], and Giani et al. (ZT ~ 0.69) [18], fabricated by co-evaporation, thermal co-evaporation, metal-organic chemical vapor deposition process, respectively (in all the cases, the thermal conductivity was assumed as 1.5 $Wm^{-1}K^{-1}$ for calculating ZT). Again, the present ZT value is in good agreement with the results obtained by Zybala et al. [16], both at room temperature and 370 K; even their synthesis procedure was different and more complex. On

the other hand, the ZT value of our thermally annealed $Sb_2Te_3$ nanostructures obtained by 10 h ball milling is superior to the ZT values reported by Wanarattikanet al. [34], for their $Sb_2Te_3$ thin films. The ZT value of ~0.5 with the present sample is superior compared to that obtained (~0.1−0.2) for thin films measured at 365 K. In the present work, the maximum obtained ZT value of 10 h milled thermally annealed $Sb_2Te_3$ is 0.543 at 370 K. Thus, this work demonstrates a comparable and even better thermoelectric performance of $Sb_2Te_3$ nanostructures than the previous reports, along with a more simple, time-efficient synthesis method using the least number of ingredients.

## 5. Conclusions

We demonstrate the fabrication of $Sb_2Te_3$ nanoparticles of different sizes utilizing a fast and straightforward mechanical alloying

process. The reaction between Sb and Te powders initiates within 1 h of milling, and single-phase rhombohedral (with hexagonal setting) $Sb_2Te_3$ is fully formed within 3 h of ball milling. Prolonged milling produces $Sb_2Te_3$ nanoparticles of smaller grain sizes, with the introduction of higher lattice strain due to severe plastic deformation of the rhombohedral lattice. Thermal annealing in an inert atmosphere induces a reduction of lattice strain and grain growth in the nanostructures and a drastic enhancement of their electrical conductivity—a transformation from typical semiconductor to metallic or degenerate semiconducting behavior was happened due to annealing. Obtained positive values of the Seebeck coefficient, indicating the p-type nature of the sample increases with milling time and also decreases on the course of annealing. It is associated with reducing particle size during milling and growth of grains via thermal treatment, respectively. There is a substantial ~ ten times increase of the power factor (from $\sim 10^{-5}$ unit to $\sim 10^{-4}$ unit) after annealing. In thermal conductivity calculation, the non-parabolic single Kane band model is used, where the Lorenz number is not a constant but a function of temperature to obtain more practical results. The much more dominant effect of thermal conductivity than electrical conductivity and Seebeck coefficient on the thermoelectric figure of merit causes a drastic increase in ZT of 10 h milled annealed sample compared to 3 h and 5 h milled samples. The lowest ZT value of 5 h milled, annealed sample is due to its highest thermal conductivity associated with the predominating phonon-charge carrier scattering effect. The increasing nature of the figure of merit curves with temperature indicates better performances at higher temperatures. Thermal annealing causes ~10 times increase in ZT of 10 h milled $Sb_2Te_3$ (from 0.039 to 0.468 at room temperature and from 0.061 to 0.543 at 370 K), primarily due to the predominating effect of enormous electrical conductivity ($\sigma$) over S and K.

## CRediT authorship contribution statement

**Shrabani Paul:** Investigation, Conceptualization, Methodology, Formal analysis, Writing - original draft. **Umapada Pal:** Conceptualization, Visualization, Writing - review & editing, Investigation, Resources. **Swapan Kumar Pradhan:** Conceptualization, Visualization, Writing - review & editing, Supervision, Validation.

## Declaration of competing interest

The authors declare that they have no known competing financial interests or personal relationships that could have appeared to influence the work reported in this paper.

## Acknowledgments

## Appendix A. Supplementary data

Supplementary data related to this article can be found at https://doi.org/10.1016/j.jallcom.2020.157732.

## References

[1] G.J. Snyder, E.S. Toberer, Complex thermoelectric materials, Nat. Mater. 7 (2008) 105−114.

[2] X. Zhang, L.D. Zhao, Thermoelectric materials: energy conversion between heat and electricity, J. Materiomics 1 (2015) 92−105.

[3] L.P. Hu, T.J. Zhu, Y.G. Wang, H.H. Xie, Z.J. Xu, X.B. Zhao, Shifting up the optimum figure of merit of p-type bismuth telluride-based thermoelectric materials for power generation by suppressing intrinsic conduction, NPG Asia Mater. 6 (2014) 1−8.

[4] J.-C. Zheng, Recent advances on thermoelectric materials, Front. Phys. China 3 (2008) 269−279.

[5] J.-F. Li, W.-S. Liu, L.-D. Zhao, M. Zhou, High-performance nanostructured thermoelectric materials, NPG Asia Mater. 2 (2010) 152−158.

[6] M. Markov, X. Hu, H.C. Liu, N. Liu, S.J. Poon, K. Esfarjani, M. Zebarjadi, Semimetals as potential thermoelectric materials, Sci. Rep. 8 (2018) 9876−9886.

[7] W. Jones, N.H. March, Theoretical Solid State Physics, Courier Dover Publications, 1985.

[8] M. Kumar, Thermoelectric properties of semiconducting materials, IOSR J. Electron. Commun. Eng. 13 (2018) 01−03.

[9] Z.-G. Chen, G. Han, L. Yang, L. Cheng, J. Zou, Nanostructured thermoelectric materials: current research and future challenge, Prog. Nat. Sci.: Mat. Int. 22 (2012) 535−549.

[10] X. Yan, B. Poudel, Y. Ma, W.S. Liu, G. Joshi, H. Wang, Y. Lan, D. Wang, G. Chen, Z.F. Ren, Experimental studies on anisotropic thermoelectric properties and structures of n-type $Bi_2Te_{2.7}Se_{0.3}$, Nano Lett. 10 (2010) 3373−3378.

[11] M. Takashiri, S. Tanaka, H. Hagino, K. Miyazaki, Combined effect of nanoscale grain size and porosity on lattice thermal conductivity of bismuth-telluride-based bulk alloys, J. Appl. Phys. 112 (2012) 084315−084322.

[12] M. Takashiri, S. Tanaka, H. Hagino, K. Miyazaki, Strain and grain size effects on thermal transport in highly-oriented nanocrystalline bismuth antimony telluride thin films, Int. J. of Heat and Mass Transfer. 76 (2014) 376−384.

[13] N.-W. Park, W.-Y. Lee, J.-E. Hong, T.-H. Park, S.-G. Yoon, H. Im, H.S. Kim, S.-K. Lee, Effect of grain size on thermal transport in post-annealed antimony telluride thin films, Nanoscale Res. Lett. 10 (2015) 1−9.

[14] P. Lošt'ák, Č. Drašar, J. Horák, Z. Zhou, J.S. Dyck, C. Uher, Transport coefficients and defect structure of $Sb_{2-x}Ag_xTe_3$ single crystals, J. Phy. Chem. Solids 67 (2016) 1457−1463.

[15] T. Khumtong, P. Sukwisute, A. Sakulkalavek, R. Sakdanuphab, Microstructure and electrical properties of antimony telluride thin films deposited by RF magnetron sputtering on flexible substrate using different sputtering pressures, J. Electron. Mater. 46 (2017) 3166−3171.

[16] R. Zybała, K. Mars, A. Mikuła, J. Bogusławski, G. Soboń, J. Sotor, M. Schmidt, K. Kaszyca, M. Chmielewski, L. Ciupiński, K. Pietrzak, Synthesis and characterization of antimony telluride for thermoelectric and optoelectronic applications, Arch. Metall. Mater. 62 (2017) 1067−1070.

[17] R. Venkatasubramanian, T. Colpitts, E. Watko, M. Lamvik, N. El-Masry, MOCVD of Bi2Te3, Sb2Te3 and their superlattice structures for thin-film thermoelectric applications, J. Cryst. Growth 170 (1997) 817−821.

[18] A. Giani, A. Boulouz, F. Pascal-Delannoy, A. Foucaran, E. Charles, A. Boyer, Growth of $Bi_2Te_3$ and $Sb_2Te_3$ thin films by MOCVD, Mater. Sci. Eng. B 64 (1999) 19−24.

[19] H. Zou, D.M. Rowe, S.G.K. Williams, Peltier effect in a co-evaporated $Sb_2Te_3$(P)-$Bi_2Te_3$(N) thin film thermocouple, Thin Solid Films 408 (2002) 270−274.

[20] N.G. Patel, P.G. Patel, Electrical properties of polycrystalline $Sb_2Te_3$ films, J. Mater. Sci. 26 (1991) 2543−2546.

[21] İ.Y. Erdoğan, Ü. Demir, Synthesis and characterization of $Sb_2Te_3$ nanofilms via electrochemical co-deposition method, J. Electroanal. Chem. 633 (2009) 253−259.

[22] P. Fan, Z.H. Zheng, G.X. Liang, X.M. Cai, D.P. Zhang, Composition-dependent characterization of $Sb_2Te_3$ thin films prepared by ion beam sputtering deposition, Chin. Phys. Lett. 27 (2010) 087021−087024.

[23] Y.K. Kim, A. Divenere, G.K. Wong, J.B. Ketterson, S. Cho, J.R. Meyer, Structural and thermoelectric transport properties of thin films grown by molecular beam epitaxy, J. Appl. Phys. 91 (2002) 715−718.

[24] S. Heimann, S. Schulz, J. Schaumann, A. Mudring, J. Stötzel, F. Maculewicze, G. Schierning, Record figure of merit values of highly stoichiometric $Sb_2Te_3$ porous bulk synthesized from tailor-made molecular precursors in ionic liquids, J. Mater. Chem. C 3 (2015) 10375−10380.

[25] C. Kim, D.-H. Kim, Y.S. Han, J.S. Chung, H. Kim, ChemInform abstract: fabrication of antimony telluride nanoparticles using a brief chemical synthetic process under atmospheric conditions, J. Alloys Comp. 509 (2011) 609−613.

[26] M. Zakeri, M. Allahkarami, Gh Kavei, A. Khanmohammadian, M.R. Rahimipour, Low temperature synthesis of nanocrystalline $Sb_2Te_3$ by mechanical alloying, J. Mater. Sci. 43 (2008) 1638−1643.

[27] M. Bumrungpon, K. Hirota, K. Takagi, K. Hanasaku, T. Hirai, I. Morioka, R. Yasufuku, M. Kitamura, K. Hasezaki, Synthesis and thermoelectric properties of bismuth antimony telluride thermoelectric materials fabricated at various ball-milling speeds with yttria-stabilized zirconia ceramic vessel and balls, Ceram. Int. 46 (2020) 13869−13876.

[28] R. Venkatasubramanian, E. Siivola, T. Colpitts, B. O'Quinn, Thin-film thermoelectric devices with high room-temperature figures of merit, Nature 413 (2001) 597−602.

[29] T.C. Harman, P.J. Taylor, M.P. Walsh, B.E. LaForge, Quantum dot superlattice

S. Paul, U. Pal and S.K. Pradhan

thermoelectric materials and devices, Science 297 (2002) 2229−2232.

[30] K.F. Hsu, S. Loo, F. Guo, W. Chen, J.S. Dyck, C. Uher, T. Hogan, E.K. Polychroniadis, M.G. Kanatzidis, Cubic AgPb$_m$SbTe$_{2+m}$: bulk thermoelectric materials with high figure of merit, Science 303 (2004) 818−821.

[31] W. Kim, J. Zide, A. Gossard, D. Klenov, S. Stemmer, A. Shakouri, A. Majumdar, Thermal conductivity reduction and thermoelectric figure of merit increase by embedding nanoparticles in crystalline semiconductors, Phys. Rev. Lett. 96 (2006) 045901−045904.

[32] X. Tang, W. Xie, H. Li, W. Zhao, Q. Zhang, M. Niino, Preparation and thermoelectric transport properties of high-performance p-type Bi2Te3 with layered nanostructure, Appl. Phys. Lett. 90 (2007) 012102−012104.

[33] S. Morikawa, T. Inamoto, M. Takashiri, Thermoelectric properties of nanocrystalline Sb2Te3 thin films: experimental evaluation and first-principles calculation, addressing effect of crystal grain size, Nanotechnol. 29 (2018) 075701.

[34] P. Wanarattikan, P. Jitthammapirom, R. Sakdanuphab, A. Sakulkalavek, Effect of grain size and film thickness on the thermoelectric properties of flexible Sb$_2$Te$_3$ thin films, Adv. Mater. Sci. Eng. 2019 (2019) 1−7.

[35] J. Chen, T. Sun, D.H. Sim, H. Peng, H. Wang, S. Fan, H.H. Hng, J. Ma, F.Y.C. Boey, S. Li, M.K. Samani, G. Chung, K. Chen, X. Chen, T. Wu, Q. Yan, Sb$_2$Te$_3$ Nanoparticles with enhanced Seebeck coefficient and low thermal conductivity, Chem. Mater. 22 (2010) 3086−3092.

[36] P. Dharmaiah, H.-S. Kim, C.-H. Lee, S.-J. Hong, Influence of powder size on thermoelectric properties of p-type 25% Bi2Te3-75% Sb2Te3 alloys fabricated using gas-atomization and spark-plasma sintering, J. Alloys Compd. 686 (2016) 1−8.

[37] J.H. Son, M.W. Oh, B.S. Kim, S.D. Park, B.K. Min, M.H. Kim, H.W. Lee, Effect of ball milling time on the thermoelectric properties of p-type (Bi,Sb)$_2$Te$_3$, J. Alloys Compd. 566 (2013) 168−174.

[38] L. Lü, M.O. Lai, Densification, Mechanical Alloying, Springer, Boston, 1998, pp. 173−187.

[39] B. Fang, Z. Zeng, X. Yan, Z. Hu, Effects of annealing on thermoelectric properties of Sb2Te3 thin films prepared by radio frequency magnetron sputtering, J. Mater. Sci. 24 (2013) 1105−1111.

[40] J. Yang, T. Aizawa, A. Yamamoto, T. Ohta, Thermoelectric properties of p-type (Bi Te )$_x$ (SbTe )$_{1-x}$ prepared via bulk mechanical alloying and hot pressing, J. Alloys Comp. 309 (2000) 225−228.

[41] L. Han, S.H. Spangsdorf, N.V. Nong, L.T. Hung, Y.B. Zhang, H.N. Pham, Y.Z. Chen, A. Roch, L. Stepien, N. Pryds, Effects of spark plasma sintering conditions on the anisotropic thermoelectric properties of bismuth antimony telluride, RSC Adv. 6 (2016) 59565−59573.

[42] S.-S. Lim, J.-H. Kim, B. Kwon, S.K. Kim, H.-H. Park, K.-S. Lee, J.M. Baik, W.J. Choi, D.-I. Kim, D.-B. Hyun, J.-S. Kim, S.-H. Baek, Effect of spark plasma sintering conditions on the thermoelectric properties of (Bi$_{0.25}$Sb$_{0.75}$)$_2$Te$_3$ alloys, J. Alloys Compd. 678 (2016) 396−402.

[43] D.-H. Lee, J.-U. Lee, S.-J. Jung, S.-H. Baek, J.-H. Kim, D.-I. Kim, D.-B. Hyun, J.-S. Kim, Effect of heat treatment on the thermoelectric properties of bismuth−antimony−telluride prepared by mechanical deformation and mechanical alloying, J. Electron. Mater. 43 (2014) 2255−2261.

[44] H.M. Rietveld, A profile refinement method for nuclear and magnetic structures, J. Appl. Crystallogr. 2 (1969) 65−71.

[45] R.A. Young, D.B. Wiles, Profile shape functions in Rietveld refinements, J. Appl. Crystallogr. 15 (1982) 430−438.

[46] H. Dutta, S.K. Pradhan, M. De, Microstructural evolution on ball-milling elemental blends of Ni, Al and Ti by Rietveld's method, Mater. Chem. Phys. 74 (2002) 167−176.

[47] L. Lutterotti, P. Scardi, P. Maistrelli, Lsi - a computer program for simultaneous refinement of material structure and microstructure, J. Appl. Crystallogr. 25 (1992) 459−462.

[48] S. Dutta, S. Bandyopadhyay, A. Dutta, S.K. Pradhan, Microstructure and electrical transport phenomenon of yttria alloyed nanocrystalline ceria solid solution synthesized by mechanical alloying, Mater. Res. Bull. 93 (2017) 333−341.

[49] S. Bid, S.K. Pradhan, Preparation and microstructure characterization of ball-milled ZrO$_2$ powder by the Rietveld method: monoclinic to cubic phase transformation without any additive, J. Appl. Cryst. 35 (2002) 517−525.

[50] S. Sain, S. Patra, S.K. Pradhan, Quickest ever single-step mechanosynthesis of Cd$_{0.5}$Zn$_{0.5}$S quantum dots: nanostructure and optical characterizations, Mater. Res. Bull. 47 (2012) 1062−1072.

[51] A. Sen, T. Kar, S.K. Pradhan, One step quickest mechanosynthesis of nanocrystalline Ti$_{0.9}$Si$_{0.1}$C and its microstructure characterization, J. Alloys Comp. 557 (2013) 47−52.

[52] A. Dhara, S. Sain, S. Das, S.K. Pradhan, Microstructure, optical, dielectric and electrical characterizations of Mn doped ZnO nanocrystals synthesized by mechanical alloying, Ceram. Int. 44 (2018) 7110−7121.

[53] K. Kaviyarasu, D. Sajan, P.A. Devarajan, A rapid and versatile method for solvothermal synthesis of Sb2O3nanocrystals under mild conditions, Appl.

[54] K. Sharma, A. Kumar, N. Goyal, M. Lal, Characterization and optical properties of Bi$_2$Te$_3$ and (Bi$_{.20}$Sb$_{.80}$)$_2$Te$_3$, AIP Adv. 1536 (2013) 603−604.

[55] K. Sharma, M. Lal, V.K. Gumber, A. Kumar, N. Chaudary, N. Goyal, Effect of composition on optical and thermoelectric properties of microstructured p-type (Bi$_2$Te$_3$)$_x$(Sb$_2$Te$_3$)$_{1-x}$ alloys, J. Nano Electr. Phy. 6 (2014) 01007−01012.

[56] U.O. Aroke, A. Abdulkarim, R.O. Ogubunka, Fourier-transform infrared characterization of kaolin, granite, bentonite and barite, ATBU, J. Environ. Technol. 6 (2013) 42−53.

[57] R.M. Silverstein, G.C. Bassler, T.C. Morrill, Spectrometric Identification of Organic Compounds, fourth ed., John Wiley and Sons, New York, 1981.

[58] K. Rajasekar, A. Subbarayan, R. Sathyamoorthy, J. Dheepa, Structural and optical properties of thermally evaporated antimony telluride thin films, Ionics 10 (2004) 291−294.

[59] J. Black, E.M. Conwbll, I. Seigle, C.W. Spencer, Electrical and optical properties of some M$_2^{V-B}$N$_3^{VI- B}$ semiconductors, J. Phys. Chem. Sol. 2 (1957) 240−251.

[60] L.P. Hu, T.J. Zhu, X.Q. Yue, X.H. Liu, Y.G. Wang, Z.J. Xu, X.B. Zhao, Enhanced figure of merit in antimony telluride thermoelectric materials by In−Ag co-alloying for mid-temperature power generation, Acta Mater. 85 (2015) 270−278.

[61] D.L. Medlin, G.J. Synder, Interfaces in bulk thermoelectric materials: a review for current opinion in colloid and interface science, Curr. Opin. Colloid Interface Sci. 14 (2009) 226−235.

[62] L.M. Goncalves, C. Couto, P. Alpuim, D.M. Rowe, J.H. Correia, Thermoelectric properties of Bi2Te3/Sb2Te3 thin films, Mater. Sci. Forum 514−516 (2006) 156−160.

[63] J.-H. Kim, J.-Y. Choi, J.-M. Bae, M.-Y. Kim, T.-S. Oh, Thermoelectric characteristics of n-Type Bi$_2$Te$_3$ and p-Type Sb$_2$Te$_3$ thin films prepared by co-evaporation and annealing for thermopile sensor applications, Mater. Transactions 54 (2013) 618−625.

[64] A.F. May, J.P. Fleurial, G.J. Snyder, Thermoelectric performance of lanthanum telluride produced via mechanical alloying, Phys. Rev. B 78 (2008) 125205−125216.

[65] S. Ahmad, S.D. Mahanti, Energy and temperature dependence of relaxation time and Wiedemann-Franz law on PbTe, Phys. Rev. B 81 (2010) 165203−165213.

[66] E.O. Kane, Semiconductors and semimetals, in: R.K. Willardson, A.C. Beer Academic (Eds.) Vol. 1, 1975. Chap. 3, New York.

[67] H.-S. Kim, Z.M. Gibbs, Y. Tang, H. Wang, G.J. Snyder, Characterization of Lorenz number with Seebeck coefficient measurement, Apl. Mater. 3 (2015) 041506−041510.

[68] C.-H. Su, Experimental determination of lattice thermal conductivity and Lorenz number as functions of temperature for n-type PbTe, Mater, Today Phys 5 (2018) 58−63.

[69] J.R. Drabble, H.J. Goldsmid, Thermal Conduction in Semiconductors, vol. 4, Oxford: Pergamon Press, Newyork, 1961.

[70] L. Hu, Y. Zhang, H. Wu, Y. Liu, J. Li, J. He, W. Ao, F. Liu, S.J. Pennycook, X. Zeng, Synergistic compositional−mechanical effects are leading to a record high ZT in n-type V$_2$VI$_3$ alloys through progressive hot deformation, Adv. Funct. Mater. 28 (2018) 1803617−1803629.

[71] K.T. Kim, H.M. Lee, D.W. Kim, K.J. Kim, G.H. Ha, G.G. Lee, Bismuth-telluride thermoelectric nanoparticles synthesized by using a polyol process, J. Korean Phys. Soc. 57 (2010) 1037−1040.

[72] M. Gharsallah, F.S. Sanchez, J. Bermudez, N.M. Nemes, J.L. Martinez, F. Elhalouani, J.A. Alonso, Nanostructured Bi$_2$Te$_3$ prepared by a straightforward arc-melting method, Nanoscale Res. Lett. 11 (2016) 1−7.

[73] M. Saleemi, M.S. Toprak, S. Li, M. Johnson, M. Muhammed, Synthesis, processing, and thermoelectric properties of bulk nanostructured bismuth telluride (Bi$_2$Te$_3$), J. Mater. Chem. 22 (2012) 725−730.

[74] C. Suryanarayana, N. Al-Aqeeli, Mechanically alloyed nanocomposites, Prog. Mater. Sci. 58 (2013) 383−502.

[75] B. Poudel, Q. Hao, Y. Ma, Y. Lan, A. Minnich, B. Yu, X. Yan, D. Wang, A. Muto, D. Vashaee, X. Chen, J. Liu, M.S. Dresselhaus, G. Chen, Z. Ren, High-thermoelectric performance of nanostructured bismuth antimony telluride bulk alloys, Science 320 (2008) 634−638.

[76] Y. Ma, Q. Hao, B. Poudel, Y. Lan, B. Yu, D. Wang, G. Chen, Z. Ren, Enhanced thermoelectric figure-of-merit in p-type nanostructured bismuth antimony tellurium alloys made from elemental chunks, Nano Lett. 8 (2008) 2580−2584.

[77] M. Singh, K.K. Hlabana, S. Singhal, K. Devlal, Grain-size effects on the thermal conductivity of nanosolids, J. Taibah Univ. Sci. 10 (2015) 375−380.

[78] Y. Wu, Z. Chen, P. Nan, F. Xiong, S. Lin, X. Zhang, Y. Chen, L. Chen, B. Ge, Y. Pei, Lattice strain advances thermoelectrics, Joule 3 (2019) 1276−1288.

[79] S.-Y. Yue, R. Yang, B. Liao, Controlling thermal conductivity of two-dimensional materials via externally induced phonon-electron interaction, Phys. Rev. B 100 (2019) 115408−115415.